crystals

MDPI

Article

Effects of Nitrogen Content and Strain Rate on the Tensile Behavior of High-Nitrogen and Nickel-Free Austenitic Stainless Steel

Feng Shi [1], Xinyue Zhang [1], Tianzeng Li [1], Xianjun Guan [1], Xiaowu Li [1,2,*] and Chunming Liu [3]

1 Department of Materials Physics and Chemistry, School of Materials Science and Engineering, Northeastern University, Shenyang 110819, China
2 State Key Laboratory of Rolling and Automation, Northeastern University, Shenyang 110819, China
3 Key Laboratory for Anisotropy and Texture of Materials, Ministry of Education, Northeastern University, Shenyang 110819, China
* Correspondence: xwli@mail.neu.edu.cn

Abstract: The uniaxial tensile behaviors of Fe-19Cr-16Mn-2Mo-0.49N and Fe-18Cr-16Mn-2Mo-0.85N high-nitrogen and nickel-free austenitic stainless steels at two strain rates of 10^{-2} s^{-1} and 10^{-4} s^{-1} were comparatively investigated. The related deformation microstructure was characterized and fracture mechanism was analyzed. The results show that the nitrogen content and strain rate both have significant effects on the tensile properties of the tested steels. As the strain rate is the same, the tested steel containing a higher nitrogen content has higher R_m and $R_{p0.2}$. However, R_m is higher at a lower strain rate and $R_{p0.2}$ is higher at a higher strain rate in the case of the same nitrogen content. The tested steel with a lower nitrogen content (0.49 wt.%N) tensioned at a lower strain rate of 10^{-4} s^{-1} obtains the highest elongation, while the tested steel with a higher nitrogen content (0.85 wt.%N) tensioned at a higher strain rate of 10^{-2} s^{-1} has the lowest elongation. The tensile plastic deformation is mainly governed by slip and twinning, affected jointly by stacking fault energy and short-range order. Dislocation slip featured by planar slip bands and twin-like bands is the main deformation structure in the tested steel containing a higher nitrogen content (0.85 wt.%N) tensioned at a lower strain rate of 10^{-4} s^{-1}, whereas twinning deformation becomes more prominent with decreasing nitrogen content and increasing strain rate.

Keywords: austenitic stainless steel; nitrogen content; strain rate; tensile property; stacking fault energy; short-range order

check for updates

Citation: Shi, F.; Zhang, X.; Li, T.; Guan, X.; Li, X.; Liu, C. Effects of Nitrogen Content and Strain Rate on the Tensile Behavior of High-Nitrogen and Nickel-Free Austenitic Stainless Steel. *Crystals* **2023**, *13*, 129. https://doi.org/10.3390/cryst13010129

Academic Editor: Wojciech Polkowski

Received: 7 December 2022
Revised: 3 January 2023
Accepted: 5 January 2023
Published: 11 January 2023

1. Introduction

The traditional austenitic stainless steels (ASSs) stabilized with Nickel are undesirable because of their expensive cost, low strength and irritability to human organs (Nickel > 0.2%) [1,2]. In recent years, researchers have developed a high-nitrogen and nickel-free ASS using nitrogen and manganese instead of nickel [3–6]. As austenite-stabilizing elements, nitrogen and manganese are added into ASS to replace the more expensive nickel, which not only solves the problem of nickel allergy but also significantly reduces the cost of the material. Moreover, the addition of nitrogen can also improve the strength and the resistance to localized corrosion of ASS [7–10]. Therefore, compared with the traditional ASS, high-nitrogen and nickel-free ASS has many more excellent properties, such as high strength, high toughness, high strain hardening ability, good corrosion resistance and low magnetization, which gives the advanced material a broad application prospect in transportation, construction, ocean engineering, biomedicine and other fields [11–15].

As an important new structural material, it is very necessary to study the mechanical properties and the relevant influencing factors of high nitrogen and nickel-free ASS. At present, there are some studies on ASS containing nitrogen and high nitrogen [16–22]. Masumura et al. [16] investigated the effect of the nitrogen content (0.001–0.2 wt.%) on the work hardening behavior in metastable Fe-18Cr-8Ni ASS and found that the increase in nitrogen content improved the work hardening of the steel. Byrnes et al. [17] studied the effect of the nitrogen content (0.04–0.36 wt.%) on the mechanical properties of stable Fe-Cr-Ni-Mo ASS and concluded that low-temperature flow stress of the tested steel increased with the increasing of the nitrogen content in solution and the decreasing of the temperature. Soussan et al. [18] investigated the effect of the nitrogen content (0–0.3 wt.%) on the work hardening behavior in type AISI 316L and 316LN ASSs and found that the yield stress and ultimate tensile stress of the tested steels increased linearly with the increase in the nitrogen content. Wang et al. [19] studied the effect of cold deformation on the microstructure and mechanical behavior of Fe-17.67Cr-12.75Mn-2.39Mo-1.2N high-nitrogen ASS, and the results showed that the work hardening index of the steel decreases with the increase in cold deformation, and the tensile deformation is easier to be carried out by the cross slip of dislocations. Shin et al. [20] studied the mechanical behavior of Fe-18Cr-18.7Mn-0.51N high-nitrogen ASS under different cold compression rates, and the results demonstrated that the tensile strength and yield strength increased with the increase in cold compression rate. Sun et al. [21] studied the influence of the cold rolling strain on the tensile properties in Fe-22Cr-17Mn-2.43Mo-0.83N high-nitrogen ASS and reported that the strength of the alloy sharply increased, but the ductility declined with the increase in the cold rolling strain amount. Saller et al. [22] studied the microstructures in the cold deformed Fe-21Cr-23Mn-0.5Mo-0.9N high-nitrogen ASS and observed planar slip dislocation structures. According to the above research findings, it can be seen that extensive research has focused on the mechanical properties of ASS containing nitrogen and cold-worked high nitrogen ASS.

In view of this, the paper will concentrate on the combined impacts of the nitrogen content and the strain rate on the mechanical properties of the high-nitrogen and nickel-free ASS, and the relevant deformation behavior and fracture mechanism will be discussed in order to provide a valuable basis for the application of this new advanced material.

2. Experimental Procedures

The tested steels used in the present study were melted by induction furnace and electroslag remelting furnace both filled with N_2. After being forged at 1473 K, the cast ingot was hot-rolled at 1373 K into a plate with 6 mm thickness and then cold rolled into plates with 4 mm thickness. The chemical compositions of the tested steels are shown in Table 1, where the two tested steels are, respectively, named Fe-19Cr-16Mn-2Mo-0.49N and Fe-18Cr-16Mn-2Mo-0.85N steels. The cold-rolled plates were solid solution treated at 1050 °C for 1 h followed by water quenching. The initial microstructures are shown in Figure 1. As shown in Figure 1a,b, the microstructures of two tested steels after solid solution treatment both show fully austenitic grains. The grain boundaries are clean, straight and thin. A few twins are observed in the microstructures. The average grain size (27.15 μm) of Fe-19Cr-16Mn-2Mo-0.49N steel is larger than that (14.47 μm) of Fe-18Cr-16Mn-2Mo-0.85N steel.

Table 1. Chemical compositions of the tested steels (wt.%).

	Cr	Mn	Mo	N	C	Fe
Fe-19Cr-16Mn-2Mo-0.49N	19.30	15.96	2.25	0.49	0.011	Balanced
Fe-18Cr-16Mn-2Mo-0.85N	18.36	16.52	2.32	0.85	0.023	Balanced

The plates after solid solution treatment were machined into the tensile specimens with a gauge section of 30 mm × 10 mm × 2 mm. Tensile tests were carried out in an AG-X plus 100 KN universal testing machine at room temperature with two initial strain rates of 10^{-4} s^{-1} and 10^{-2} s^{-1}. Three specimens were used for each condition and the average value of these three data is the final measured value. The microstructures were observed by an optical microscope (OM), and fracture surface features of the samples were observed by a JSM-7001F scanning electron microscope (SEM). Thin foils for the transmission electron microscopy (TEM) observation were prepared using a twin-jet electrolytic polisher, operated at 20 V in an electrolyte of perchloric acid and alcohol at −25 °C. Morphology and crystallography of microstructures near the fracture were examined by JEM-2100F TEM.

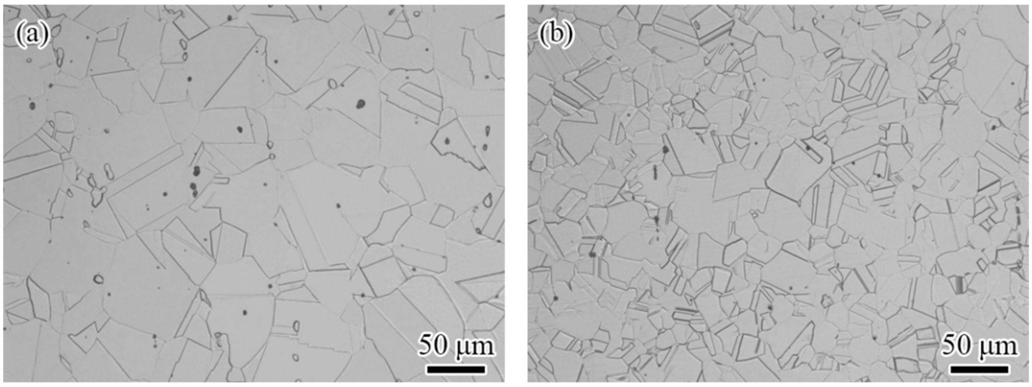

Figure 1. OM images showing the initial microstructures in the Fe-19Cr-16Mn-2Mo-0.49N (**a**) and Fe-18Cr-16Mn-2Mo-0.85N (**b**) steels.

3. Results

3.1. Mechanical Properties

Figure 2 shows the engineering stress–strain curves of the tested steels at two strain rates of 10^{-4} s^{-1} and 10^{-2} s^{-1}. In order to more clearly analyze the influences of the nitrogen content and strain rate on the tensile properties, the main tensile properties of the tested steels at different strain rates are listed in Table 2. It can be seen that the nitrogen content and strain rate both have significant effects on the tensile properties of the tested steels. For the tensile strength (R_m) and yield strength ($R_{p0.2}$), the effect of nitrogen content is much more evident than the effect of strain rate, and the tested steel containing a high nitrogen content (0.85 wt.%N) has higher R_m and $R_{p0.2}$. However, R_m is higher at a lower strain rate and $R_{p0.2}$ is higher at a higher strain rate in the case of the same nitrogen content. For the elongation after fracture (δ), the effect of the strain rate becomes dominant compared with the effect of nitrogen content, and the two tested steels deformed at the strain rate of 10^{-4} s^{-1} both have a higher δ. As the strain rate is the same, the tested steel containing a lower nitrogen content has a better ductility. Considering the joint effects of nitrogen content and strain rate, δ is the highest in the sample with a lower nitrogen content (0.49 wt.%N) at a lower strain rate (10^{-4} s^{-1}) and the lowest in the sample with a higher nitrogen content (0.85 wt.%N) at a higher strain rate (10^{-2} s^{-1}).

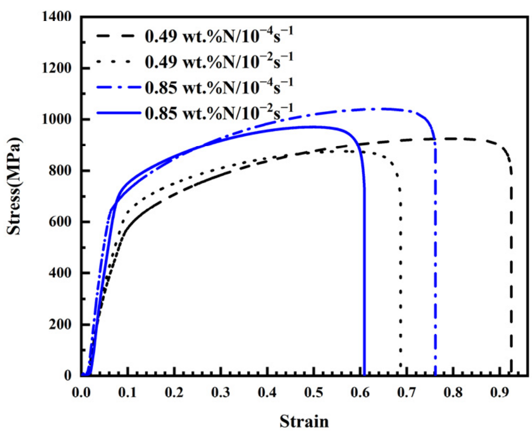

Figure 2. Engineering stress–strain curves of Fe-18Cr-16Mn-2Mo-0.85N and Fe-19Cr-16Mn-2Mo-0.49 N steels at two strain rates of 10^{-4} s^{-1} and 10^{-2} s^{-1}.

Table 2. Tensile properties of the tested steels tensioned at two strain rates.

Sample	Strain Rate, s^{-1}	R_m, MPa	$R_{p0.2}$, MPa	δ, %
Fe-19Cr-16Mn2Mo-0.49N	10^{-4}	930 ± 10.1	541 ± 3.3	66.86 ± 2.18
	10^{-2}	882 ± 13.6	559 ± 10.6	50.98 ± 1.85
Fe-18Cr-16Mn-2Mo-0.85N	10^{-4}	1037 ± 7.3	642 ± 6.5	58.01 ± 1.70
	10^{-2}	985 ± 17.5	718 ± 8.2	47.18 ± 1.56

3.2. Fracture Surface Features

Figure 3 shows the fracture surface features of the tested steels at the two strain rates of 10^{-4} s^{-1} and 10^{-2} s^{-1}. It can be found that the fibrous regions of tensile fractures are composed of dimples with different sizes. The size of large dimples is about 5~10 µm, while the size of small dimples is generally less than 1 µm (Figure 3a–c). The comparison of the dimple morphologies in the samples tensioned at different strain rates reveals that, as the nitrogen content is the same, the dimples of the sample at the lower strain rate are larger and deeper; moreover, the proportion of large-sized dimples is significantly higher. In addition, serpentine slip characteristics are found in the samples at the strain rate of 10^{-4} s^{-1}, which indicates that the plastic deformation and stress concentration occur more seriously during the formation of the dimple, and more energy is absorbed during the fracture process; therefore, the toughness and ductility are better in the samples tensioned at the lower strain rate of 10^{-4} s^{-1}. In addition, at the lower strain rate of 10^{-4} s^{-1}, the second phase particles appear in some large dimples; as marked by the arrows in Figure 3a,c, the arrows mark the second phase particles in large dimples, while this phenomenon is rarely observed at the higher strain rate of 10^{-2} s^{-1}, which shows that the tensile fracture mechanism of the tested steels at different strain rates may be different. The comparison of the dimple morphologies in the samples with different nitrogen contents reveals that, at the same strain rate, the dimples in the sample containing a lower nitrogen content are larger and deeper. Considering the joint effects of the nitrogen content and strain rate, it can be seen that in the sample with a lower nitrogen content tensioned at a lower strain rate (Figure 3a), the fracture surface is more undulating, the serpentine slip features are also more obvious and the dimples are the deepest. In contrast, in the sample with a higher nitrogen content tensioned at a higher strain rate, the dimples are small and shallow, and microareas of brittle quasi-cleavage fracture are found, as marked by the circle in Figure 3d. This is consistent with the mechanical properties listed in Table 2.

3.3. Deformation Microstructures

Figure 4 shows the tensile deformation microstructures of Fe-19Cr-16Mn-2Mo-0.49N steel at different strain rates. Figure 4a–c show the microstructures at the strain rate of 10^{-2} s^{-1}. A large number of twins arranged in parallel can be clearly observed in Figure 4a,b, and twin boundaries are very clear and complete; nearly no stacking faults are observed between the twins. Figure 4c shows that there are a lot of stacking faults and dislocation structures in between the twins arranged in parallel, which tends to form a certain number of secondary deformation twins. Figure 4d–f show the microstructures at the strain rate of 10^{-4} s^{-1}. Figure 4d shows that a large number of twins pass through several deformation bands and bend at the interface of deformation bands under the action of dislocation planar slip in the other direction, which indicates that twinning shear bears the certain plastic deformation. In Figure 4e, the appearance of deformation bands indicates that the local deformation of the sample is very severe; in this case, the dislocation slip cannot fully meet the needs of plastic deformation of materials, and twinning comes into play as another deformation mechanism. Therefore, there is a strong plastic deformation concentration around the deformation bands, which induces a large number of new deformation twins. Figure 4f shows several deformation bands and some new deformation twins. These deformation bands exhibit a similar morphologic characteristic to deformation twins, differing from those observed in Figure 4d,e; however, the relevant diffraction patterns

(Figure 4f) have indeed demonstrated that these deformation bands are not deformation twins, and they are called twin-like bands, which are reported in high-nitrogen ASS [23] and the Cu–Zn alloy [24]. The formation of these twin-like band structures is first caused by the planar slip of dislocations, and then the slip increases the width of the slip band and the dislocation density in the slip band during deformation; finally, the twin-like bands are formed. These twin-like bands are actually the initial morphologies of deformation twins [25].

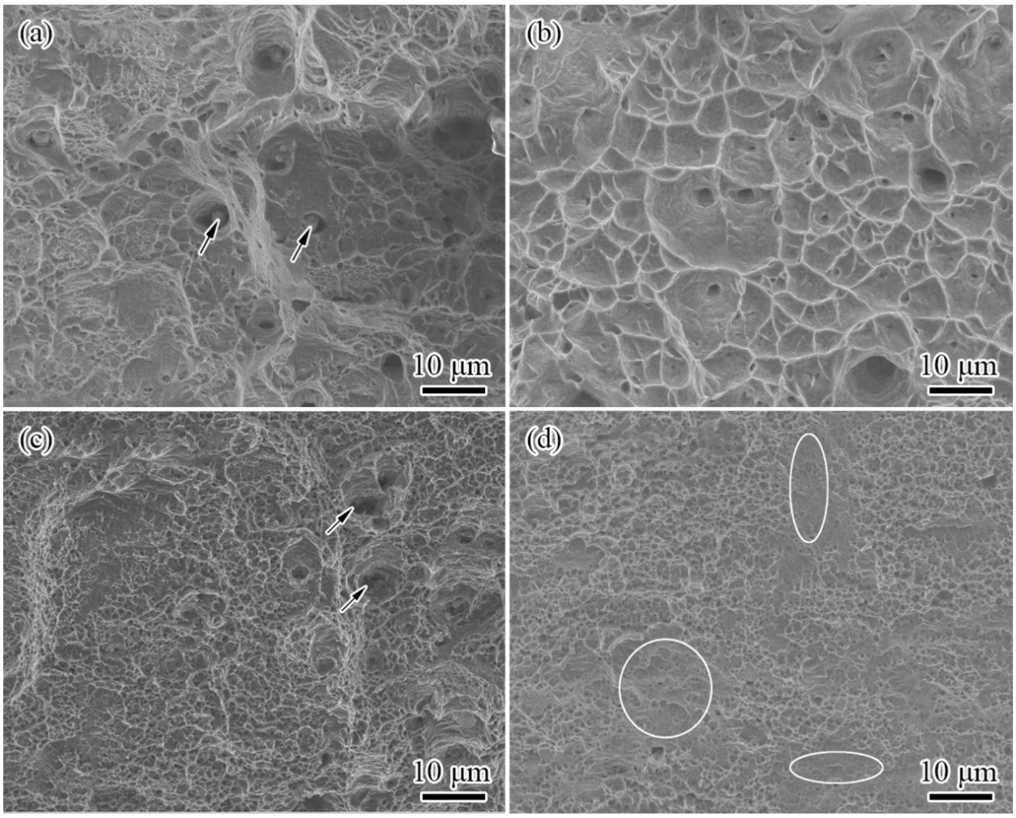

Figure 3. SEM images showing the tensile fracture surface features in Fe-19Cr-16Mn-2Mo-0.49N (**a**,**b**) and Fe-18Cr-16Mn-2Mo-0.85N (**c**,**d**) steels at the strain rates of 10^{-4} s^{-1} (**a**,**c**) and 10^{-2} s^{-1} (**b**,**d**).

Figure 5 shows the tensile deformation microstructures of Fe-18Cr-16Mn-2Mo-0.85N steel at different strain rates. At the strain rate of 10^{-2} s^{-1}, two active planar slip systems are operated, as seen in Figure 5a. This is because the grains rotate through coordination during the tensile process, making more grains orientated in the soft direction, thus leading to the initiation of more slip systems. At the same time, there are a large number of plugging dislocations between the slip planes. The dislocations belonging to different slip planes hinder each other, which leads to the further multiplication of dislocations in the slip plane. As shown in Figure 5b, interlaced twins appear in two directions with an angle of 60° in the same grain and the intersecting position of the twins has been cut and bent to some extent. It can be seen that there are high-density dislocations in or around the twins. Figure 5c shows some deformation twins crossing the grain boundary. At the strain rate of 10^{-4} s^{-1}, a large number of planar slip bands that are parallel to each other are observed, as shown in Figure 5d. The slip band contains high-density dislocations, and the dislocation density between the slip bands is slightly lower than that inside the bands. In addition, a large number of deformation twins can be observed, and a lot of planar slip bands are formed in the host twin and on both sides of the host twin, as presented in Figure 5e. In addition, some twin-like bands are observed to pile up in parallel at the grain boundary, as shown in Figure 5f.

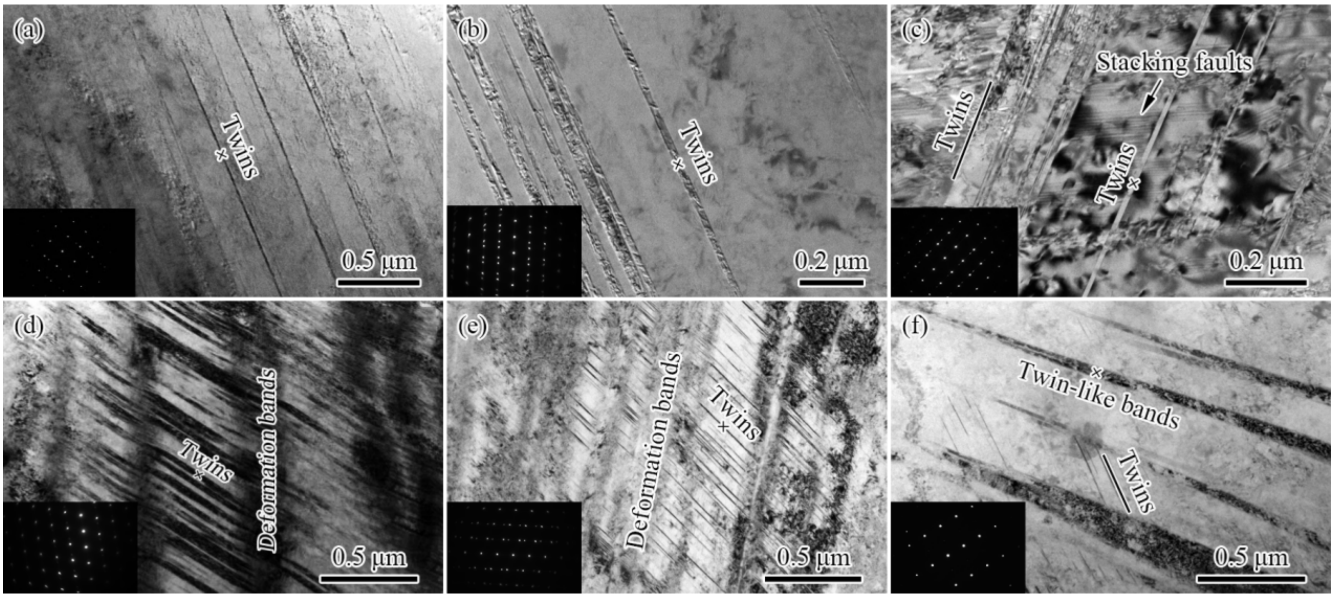

Figure 4. TEM images showing the deformation microstructures in Fe-19Cr-16Mn-2Mo-0.49N steel at the strain rates of 10^{-2} s^{-1} (**a**–**c**) and 10^{-4} s^{-1} (**d**–**f**). Note that the inset in (**a**–**f**) is the selected area diffraction pattern (SADP).

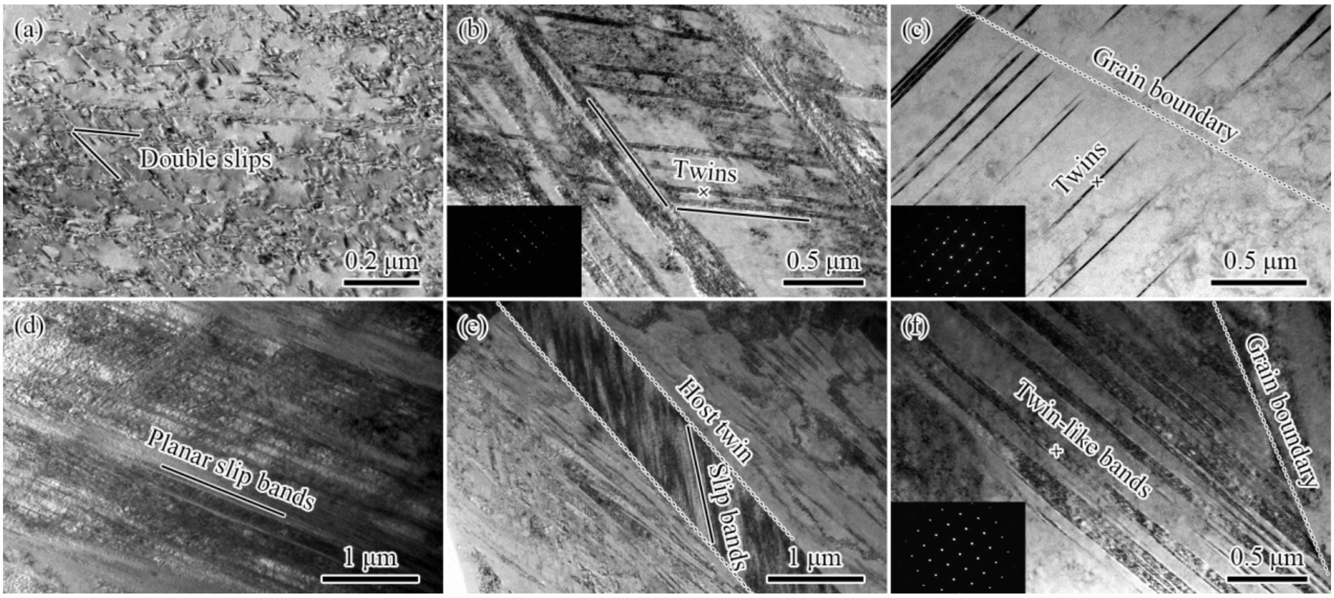

Figure 5. TEM images showing the deformation microstructures in Fe-18Cr-16Mn-2Mo-0.85N steel at the strain rates of 10^{-2} s^{-1} (**a**–**c**) and 10^{-4} s^{-1} (**d**–**f**). Note that the inset in (**b**,**c**,**f**) is the SADP.

According to TEM results of Figures 4 and 5, slip and twinning are both observed in the tested steels. However, the planar slip dislocation structure is the main microstructural feature in the tested steel containing a higher nitrogen content at a lower strain rate, while twinning is the typical plastic deformation mode in the tested steel containing a lower nitrogen content at a higher strain rate.

4. Discussion

As presented above, the nitrogen content and strain rate have a joint effect on the deformation microstructures and fracture mechanism of high nitrogen and nickel-free ASS, and consequently on their mechanical properties.

Stacking fault energy (SFE) and short-range order (SRO) are two important factors affecting the deformation microstructure in the high nitrogen ASS, and both of them often work together to affect the mechanical properties of materials [26]. The SFE of ASS is generally lower; however, the influence of the nitrogen content on the SFE is often varied [23,27,28]. For instance, Gavriljuk et al. [28] measured the SFE of Fe-15Cr-17Mn ASS with different nitrogen contents using TEM, and they found that the SFE of nickel-free steel first decreased to a minimum at 0.48 wt.%N and then increased with the increase in nitrogen content. Accordingly, it can be inferred that the SFE of the tested steel containing 0.49 wt.%N should be lower than that of the steel containing 0.85 wt.%N. The critical stress for twinning deformation is closely related to the SFE in ASS, as quantitatively expressed by Equation (1) [29]:

$$\sigma_T = 6.14\gamma_{SF}/b_p \tag{1}$$

where σ_T is the critical stress required for twinning formation, γ_{SF} is the SFE of ASS and b_p is the Burgers vector. Apparently, the critical stress for twinning deformation in ASS is proportional to the SFE. There are some controversies about the formation mechanism of deformation twins [29–32]. According to the characteristic of deformation microstructure in the tested steels (Figures 4 and 5), it can be speculated that there are two major modes for the formation of deformation twins in the tested steels under the combined action of SFE and SRO: (1) Due to the lower SFE in ASS, a lot of stacking faults are produced in the material, resulting in the formation of deformation twins during deformation [30]. (2) According to the dislocation pile-up and slip mechanism proposed by Singh et al. [31,32], the formation process of deformation twins in the tested steels may take place in sequence as follows: dislocation pile-up/slip → dislocation bands → twin-like bands → deformation twins.

The twinning deformation is dominant in the steel containing a lower nitrogen content, and this phenomenon is more obvious at a higher strain rate because the tested steel containing a lower nitrogen content owns a lower SFE, and thus a lower critical stress for the formation of deformation twins. In addition, the higher strain rate is also conducive to the formation of deformation twins [33]. Therefore, the SFE is the dominant parameter determining the deformation mechanism in the steel contain 0.49 wt.%N tensioned at the strain rate of 10^{-2} s^{-1} (Figure 4a–c), which makes twinning become the main deformation mode; moreover, the formation of most deformation twins complies with the first above-mentioned mode. In contrast, besides some deformation twins, a great amount of planar slip dislocation structures, including double slip and slip in the host twin are observed in the tested steel containing 0.85 wt.%N (Figure 5). Actually, there are a lot of SRO structures in high nitrogen ASS after a solution treatment, and the amount of SRO increases with the increase in nitrogen content [23,34,35]. The formation of planar slip dislocation structures in the tested steels is closely related to the SFE and SRO. On the one hand, due to the lower SFE in high-nitrogen ASS, a perfect dislocation is easier to dissociate into two partial dislocations (or extended dislocation) with a large equilibrium width, so that the activation energy required for the recombination of partial dislocations into a perfect dislocation is very high, profoundly restricting the cross slip of dislocations. Therefore, a large number of extended dislocations can only slip on the stacking fault plane [36]. On the other hand, nitrogen atoms can change the distribution of alloying elements in the steel through the interaction between interstitial and substitutional atoms to increase the free electron density in ASS, thus promoting the SRO formation. The SRO can effectively restrain the cross slip of dislocations and promote planar slip [26,37–40]. Therefore, the SRO is the dominant factor influencing the deformation microstructure in the steel containing 0.85 wt.% nitrogen, so that planar slip bands and twin-like bands are mainly formed in the steel containing 0.85 wt.%N tensioned at the strain rate of 10^{-4} s^{-1} (Figure 5d–f), which basically follows the second above-mentioned mode.

As can be seen from the stress–strain curves of these two steels (Figure 2), when the strain rate is the same, with the increase in nitrogen content, the $R_{p0.2}$ and R_m of the steels increase, attributing to the combined actions of fine grain strengthening [41], solution strengthening [15] and SRO strengthening [20]. The increase in the solid solubility of nitrogen can refine grains (Figure 1), cause a greater lattice distortion [15,42], enhance the SRO structure and promote planar slip of dislocation, thus improving the work hardening capacity of high-nitrogen ASS. When the nitrogen content is the same, the $R_{0.2}$ is higher but the R_m are lower in the tested steel tensioned at a higher strain rate of 10^{-2} s^{-1} than those at a lower strain rate of 10^{-4} s^{-1}, which was also observed in other high-nitrogen steels [23,43]. As two kinds of plastic deformation modes, slipping and twinning both take place in the tested steels during uniaxial tension, but the formation of deformation twins generally occurs after yielding in high-nitrogen ASS [23,30]. With the increase in strain rate, the actuation of slip system needs higher stress, resulting in the increase in $R_{0.2}$. The reduction in R_m is related to the deformation microstructures. In the steel containing a lower nitrogen content, the deformation microstructure is mainly composed of deformation twins arranged in parallel at the strain rate of 10^{-2} s^{-1} (Figure 4a–c), while deformation twins, dislocation bands and twin-like bands are observed at the strain rate of 10^{-4} s^{-1} (Figure 4d–f). In the steel containing a higher nitrogen content, the deformation microstructures are mainly featured by deformation twins and double-slip at the strain rate of 10^{-2} s^{-1} (Figure 5a–c) but by planar slip bands and twin-like bands at the strain rate of 10^{-4} s^{-1} (Figure 5d–f). Obviously, compared with the deformation microstructures at 10^{-2} s^{-1}, the interaction between dislocation bands and deformation twins in the 0.49 wt.%N steel, as well as the pilling up of twin-like bands and planar slip bands at grain boundaries and twin boundaries in the 0.85 wt.%N steel at 10^{-4} s^{-1}, would enhance the work hardening rate, and thus improve the R_m of the tested steels.

As seen in Table 2, the δ is also closely related to the nitrogen content and strain rate. The δ is the highest in the 0.49 wt.%N steel tensioned at 10^{-4} s^{-1}, but the lowest in the 0.85 wt.%N steel tensioned at 10^{-2} s^{-1}, which is attributed to the different deformation and fracture mechanisms. As mentioned above, as the nitrogen content and strain rate are both lower, some large-sized dimples with particles appear on the fracture surface, as shown in Figure 3a. In this case, microcracks are usually initiated around the particles and propagate along slip bands or grain boundaries. When these microcracks are connected with each other, the sample will eventually fracture. The tensile fracture mode of samples tensioned at 10^{-4} s^{-1} is mainly characterized by microvoid coalescence. In addition, there are many parallel deformation twins in the tested 0.49 wt.%N steel (Figure 4d–f); therefore, the sample with lower nitrogen content tensioned at lower strain rate exhibits the best ductility.

As the nitrogen content and strain rate are both higher, there are few particles in the dimples on the fracture surface (Figure 3b,d) and brittle quasi-cleavage fracture features are observable (Figure 3d). In the 0.85 wt.%N steel sample tensioned at 10^{-2} s^{-1}, crossed twins (Figure 5b) and double slip (Figure 5a) are observed, indicating that the crack may be first initiated at the intersections between primary and secondary twins, or at the intersections of slip bands, as schematically shown in Figure 6. On meeting a primary twin, the twinning dislocations of the secondary twin may form a disclination dipole. In the stress region of this dipole, coordinated dislocation motion within the primary twin (obstacle twin) occurs, thereby transferring the shear strain of the secondary twin across the obstacle twin, and consequently a microcrack is formed on the side of the obstacle twin boundary [44] (Figure 6a). In addition, slip bands in different directions were observed to appear in the sample. Microcracks are easy to nucleate at the sites where slip planes intersect and expand along the active slip plane, resulting in cracking along slip bands [45] (Figure 6b). Accordingly, the crossed twin boundaries and planar slip planes of dislocations are easy to become the sites for nucleating many microcracks, leading to a brittle quasi-cleavage fracture feature [44,45]; therefore, the ductility of the 0.85 wt.%N steel tensioned at 10^{-2} s^{-1} is the lowest.

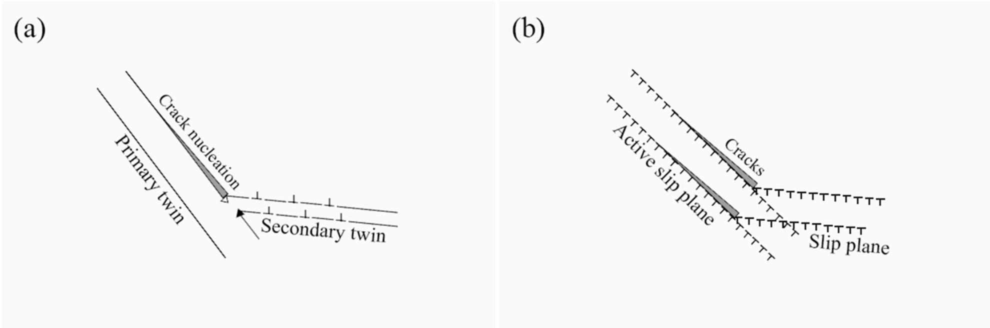

Figure 6. The schematic diagram of cracks nucleated by crossed deformation twin (**a**) and double slip of dislocations (**b**).

5. Conclusions

(1) When the nitrogen content is the same, $R_{p0.2}$ of the tested steel at the strain rate of 10^{-2} s^{-1} is higher, while R_m is higher at the strain rate of 10^{-4} s^{-1}, ascribing to different work-hardening effects produced by different deformation microstructures. At the same strain rate, $R_{p0.2}$ and R_m of the tested steel with 0.85 wt.%N are higher, which is mainly due to the combined actions of fine grain strengthening, solution strengthening and short-range order strengthening.

(2) The tested steel containing 0.49 wt.%N obtains the highest ductility tensioned at 10^{-4} s^{-1}, which is attributed to the fracture mode of microvoid coalescence and formation of many parallel deformation twins induced by lower stacking fault energy, while the ductility is the lowest in the tested steel containing 0.85 wt.%N tensioned at 10^{-2} s^{-1}, which is mainly due to the fact that the microcracks are easy to nucleate in the crossed twin boundaries and planar slip planes of dislocations, leading to a brittle quasi-cleavage fracture feature.

Author Contributions: Formal analysis, X.G.; investigation, X.Z.; re-sources, C.L.; data curation, T.L.; writing—original draft preparation, F.S.; writing—review and editing, X.L. All authors have read and agreed to the published version of the manuscript.

Funding: This work was financially supported by the National Natural Science Foundation of China (Grant Nos. 51871048 and 52171108) and the Fundamental Research Funds for the Central Universities (Grant Nos. N2002014 and N2202011).

Data Availability Statement: All data in this study are provided in the present manuscript.

Conflicts of Interest: The authors declare no conflict of interest.

References

1. Ma, T.; Wan, P.; Cui, Y.; Zhang, G.; Li, J.; Liu, J.; Ren, Y.; Yang, K.; Lu, L. Cytocompatibility of High Nitrogen Nickel-Free Stainless Steel for Orthopedic Implants. *J. Mater. Sci. Technol.* **2012**, *28*, 647–653. [CrossRef]
2. Yuan, J.P.; Li, W.; Chen, S.X.; Lu, H.X. Research and development of high nitrogen nickel-free austenitic stainless steel. *Foundry* **2012**, *61*, 1308–1312. (In Chinese)
3. Shi, F.; Gao, R.H.; Guan, X.J.; Liu, C.M.; Li, X.W. Application of grain boundary engineering to improve intergranular corro-sion resistance in a Fe–Cr–Mn–Mo–N high-nitrogen and nickel-free austenitic stainless steel. *Acta Metall. Sin. (Engl. Lett.)* **2020**, *33*, 789–798. [CrossRef]
4. Kim, J.-K.; Kwon, M.-H.; De Cooman, B.C. On the deformation twinning mechanisms in twinning-induced plasticity steel. *Acta Mater.* **2017**, *141*, 444–455. [CrossRef]
5. Li, H.; Jiang, Z.; Feng, H.; Zhang, S.; Li, L.; Han, P.; Misra, R.; Li, J. Microstructure, mechanical and corrosion properties of friction stir welded high nitrogen nickel-free austenitic stainless steel. *Mater. Des.* **2015**, *84*, 291–299. [CrossRef]
6. Shi, F.; Tian, P.; Jia, N.; Ye, Z.; Qi, Y.; Liu, C.; Li, X. Improving intergranular corrosion resistance in a nickel-free and manganese-bearing high-nitrogen austenitic stainless steel through grain boundary character distribution optimization. *Corros. Sci.* **2016**, *107*, 49–59. [CrossRef]
7. Simmons, J. Overview: High-nitrogen alloying of stainless steels. *Mater. Sci. Eng. A* **1996**, *207*, 159–169. [CrossRef]
8. Yoon, Y.-S.; Ha, H.-Y.; Lee, T.-H.; Kim, S. Effect of N and C on stress corrosion cracking susceptibility of austenitic Fe18Cr10Mn-based stainless steels. *Corros. Sci.* **2014**, *80*, 28–36. [CrossRef]

9. Simmons, J. Strain hardening and plastic flow properties of nitrogen-alloyed Fe-17Cr-(8–10)Mn-5Ni austenitic stainless steels. *Acta Mater.* **1997**, *45*, 2467–2475. [CrossRef]
10. Müllner, P.; Solenthaler, C.; Uggowitzer, P.; Speidel, M. On the effect of nitrogen on the dislocation structure of austenitic stainless steel. *Mater. Sci. Eng. A* **1993**, *164*, 164–169. [CrossRef]
11. Dai, Q.; Yuan, Z.; Chen, X.; Chen, K. High-cycle fatigue behavior of high-nitrogen austenitic stainless steel. *Mater. Sci. Eng. A* **2009**, *517*, 257–260. [CrossRef]
12. Raj, B.; Mudali, U.K. Materials development and corrosion problems in nuclear fuel reprocessing plants. *Prog. Nucl. Energy* **2006**, *48*, 283–313. [CrossRef]
13. Uggowitzer, P.; Magdowski, R.; Speidel, M.O. High Nitrogen Steels. Nickel Free High Nitrogen Austenitic Steels. *ISIJ Int.* **1996**, *36*, 901–908. [CrossRef]
14. Lo, K.H.; Shek, C.H.; Lai, J.K.L. Recent developments in stainless steels. *Mater. Sci. Eng. R Rep.* **2009**, *65*, 39–104. [CrossRef]
15. Baba, H.; Kodama, T.; Katada, Y. Role of nitrogen on the corrosion behavior of austenitic stainless steels. *Corros. Sci.* **2002**, *44*, 2393–2407. [CrossRef]
16. Masumura, T.; Tsuchiyama, T. Effect of Carbon and Nitrogen on Work-hardening Behavior in Metastable Austenitic Stainless Steel. *ISIJ Int.* **2021**, *61*, 617–624. [CrossRef]
17. Byrnes, M.; Grujicic, M.; Owen, W. Nitrogen strengthening of a stable austenitic stainless steel. *Acta Met.* **1987**, *35*, 1853–1862. [CrossRef]
18. Soussan, A.; Degallaix, S.; Magnin, T. Work-hardening behaviour of nitrogen-alloyed austenitic stainless steels. *Mater. Sci. Eng. A* **1991**, *142*, 169–176. [CrossRef]
19. Wang, S.T.; Yang, K.; Shan, Y.Y.; Li, L.F. Effect of Cold Deformation on Microstructure and Mechanical Behavior of High Nitrogen Austenitic Stainless Steel. *Acta Metall. Sin.* **2007**, *43*, 713–718.
20. Shin, J.-H.; Lee, J.-W. Effects of twin intersection on the tensile behavior in high nitrogen austenitic stainless steel. *Mater. Charact.* **2014**, *91*, 19–25. [CrossRef]
21. Sun, S.C.; Mu, J.W.; Jiang, Z.H.; Ji, C.T.; Lian, J.S.; Jiang, Q. Effect of cold rolling on tensile properties and microstructure of high nitrogen alloyed austenitic steel. *Mater. Sci. Technol.* **2013**, *30*, 146–151. [CrossRef]
22. Saller, G.; Spiradek-Hahn, K.; Scheu, C.; Clemens, H. Microstructural evolution of Cr–Mn–N austenitic steels during cold work hardening. *Mater. Sci. Eng. A* **2006**, *427*, 246–254. [CrossRef]
23. Shao, C.W.; Shi, F.; Guo, W.W.; Li, X.W. Plastic deformation and damage behaviors of Fe-18Cr-18Mn-0.63 N high-nitrogen austenitic stainless steel under uniaxial tension and compression. *Mater. Trans.* **2015**, *56*, 46–53. [CrossRef]
24. Xiao, G.H.; Tao, N.R.; Lu, K. Effects of strain, strain rate and temperature on deformation twinning in a Cu–Zn alloy. *Scr. Mater.* **2008**, *59*, 975–978. [CrossRef]
25. Jin, Z.; Bieler, T.R. An in-situ observation of mechanical twin nucleation and propagation in TiAl. *Philos. Mag. A* **1995**, *71*, 925–947. [CrossRef]
26. Wang, Z.; Han, D.; Li, X. Competitive effect of stacking fault energy and short-range clustering on the plastic deformation behavior of Cu-Ni alloys. *Mater. Sci. Eng. A* **2017**, *679*, 484–492. [CrossRef]
27. Karaman, I.; Sehitoglu, H.; Maier, H.; Chumlyakov, Y. Competing mechanisms and modeling of deformation in austenitic stainless steel single crystals with and without nitrogen. *Acta Mater.* **2001**, *49*, 3919–3933. [CrossRef]
28. Gavriljuk, V.; Petrov, Y.; Shanina, B. Effect of nitrogen on the electron structure and stacking fault energy in austenitic steels. *Scr. Mater.* **2006**, *55*, 537–540. [CrossRef]
29. Byun, T. On the stress dependence of partial dislocation separation and deformation microstructure in austenitic stainless steels. *Acta Mater.* **2003**, *51*, 3063–3071. [CrossRef]
30. Lee, T.-H.; Oh, C.-S.; Kim, S.-J.; Takaki, S. Deformation twinning in high-nitrogen austenitic stainless steel. *Acta Mater.* **2007**, *55*, 3649–3662. [CrossRef]
31. Singh, S.R.; Howe, J.M. Effect of Ta on twinning in TiAl. *Scr. Metall. Mater.* **1991**, *25*, 485–490. [CrossRef]
32. Singh, S.; Howe, J.M. Studies on the deformation behaviour of interfaces in (γ + $\alpha 2$) titanium aluminide by high-resolution transmission electron microscopy. *Philos. Mag. Lett.* **1992**, *65*, 233–241. [CrossRef]
33. Mandal, S.; Bhaduri, A.K.; Sarma, V.S. Role of Twinning on Dynamic Recrystallization and Microstructure During Moderate to High Strain Rate Hot Deformation of a Ti-Modified Austenitic Stainless Steel. *Met. Mater. Trans. A* **2012**, *43*, 2056–2068. [CrossRef]
34. Xu, M.Z.; Wang, L.J.; Wang, J.J.; Liu, C.M. Effect of nitrogen on plastic rheological behavior of New nickel-free High nitrogen austenitic Stainless Steel. *J. Mater. Metall.* **2011**, *10*, 132–135.
35. Grujicic, M. Embedded-atom/Monte Carlo study of short-range order in nitrogen strengthened Fe-Ni-Cr austenite. *Mater. Sci. Eng. A* **1994**, *177*, 233–241. [CrossRef]
36. Wang, W.; Chen, S.M.; Yan, W.; Zhao, L.J.; Shan, Y.Y.; Yang, K. Effect of Nitrogen on Microstructure of Cold Deformed High Nitrogen Austenitic Stainless Steel. *J. Mater. Heat Treat.* **2010**, *31*, 59–65.
37. Kim, J.M.; Kim, S.J.; Kang, J.H. Effects of short-range ordering and stacking fault energy on tensile behavior of nitro-gen-containing austenitic stainless steels. *Mater. Sci. Eng. A* **2022**, *836*, 142730. [CrossRef]
38. Gerold, V.; Karnthaler, H. On the origin of planar slip in F.C.C. alloys. *Acta Met.* **1989**, *37*, 2177–2183. [CrossRef]
39. Saenarjhan, N.; Kang, J.-H.; Kim, S.-J. Effects of carbon and nitrogen on austenite stability and tensile deformation behavior of 15Cr-15Mn-4Ni based austenitic stainless steels. *Mater. Sci. Eng. A* **2018**, *742*, 608–616. [CrossRef]

40. Han, D.; Zhang, Y.; Li, X. A crucial impact of short-range ordering on the cyclic deformation and damage behavior of face-centered cubic alloys: A case study on Cu-Mn alloys. *Acta Mater.* **2020**, *205*, 116559. [CrossRef]
41. Werner, E. Solid solution and grain size hardening of nitrogen-alloyed austenitic steels. *Mater. Sci. Eng. A* **1988**, *101*, 93–98.
42. Blewitt, T.H.; Coltman, R.R.; Redman, J.K. Low-Temperature Deformation of Copper Single Crystals. *J. Appl. Phys.* **1957**, *28*, 651–660. [CrossRef]
43. Li, H.-B.; Jiang, Z.-H.; Shen, M.-H.; You, X.-M. High Nitrogen Austenitic Stainless Steels Manufactured by Nitrogen Gas Alloying and Adding Nitrided Ferroalloys. *J. Iron Steel Res. Int.* **2007**, *14*, 63–68. [CrossRef]
44. Müllner, P. On the ductile to brittle transition in austenitic steel. *Mater. Sci. Eng. A* **1997**, *234–236*, 94–97. [CrossRef]
45. Tomota, Y.; Xia, Y.; Inoue, K. Mechanism of low temperature brittle fracture in high nitrogen bearing austenitic steels. *Acta Mater.* **1998**, *46*, 1577–1587. [CrossRef]